Journal of the European Ceramic Society 13 (1994) 89–102

Yttria–Ceria Stabilized Tetragonal Zirconia Polycrystals: Sintering, Grain Growth and Grain Boundary Segregation

M. M. R. Boutz, A. J. A. Winnubst* & A. J. Burggraaf

University of Twente, Faculty of Chemical Technology, Laboratory for Inorganic Chemistry, Materials Science and Catalysis, P.O. Box 217, 7500 AE Enschede, The Netherlands

(Received 23 June 1993, accepted 15 October 1993)

Abstract

An analysis is presented of grain growth and densification of yttria–ceria stabilized tetragonal zirconia polycrystals (Y,Ce TZPs) using both isothermal and non-isothermal techniques. The characteristics of Y,Ce TZPs are compared to those of Y-TZP and Ce-TZP and the effect of increasing ceria concentration at constant yttria content is evaluated. During non isothermal sintering two regimes are distinguished: below 900–1000 °C the neck area increases strongly by surface diffusion accompanied by only very little densification and grain growth, in the temperature interval 900–1000 °C to 1200 °C the materials densify to 95% of the theoretical density via a grain boundary diffusion mechanism and grain growth accelerates. Dense materials with grain sizes of 0.15–0.20 μm can be prepared by isothermal sintering at 1100–1150 °C.

In Y,Ce TZP it is yttrium that segregates to the grain boundaries at 1150–1400 °C. The yttrium content of the grain boundaries in Y,Ce-TZP is independent of temperature and ceria concentration under the investigated experimental conditions. Grain growth in dense TZP is controlled by a solute drag mechanism at elevated temperatures (> 1200 °C), this drag is highest for Y-TZP, absent for Ce-TZP and moderate for Y,Ce-TZP.

Im folgenden wird das Kornwachstum und die Verdichtung von Yttriumoxyd und Zeriumoxyd stabilisiertem, tetragonalem polykristallinem Zirkonoxyd (Y,Ce TZP) diskutiert, die mit Hilfe von isothermischen und nichtisothermischen Methoden untersucht wurden. Die Merkmale von Y,Ce TZPs werden mit denen von Y-TZP und Ce-TZP verglichen und der Effekt eines zunehmenden Zeriumoxydgehalts bei konstantem Yttriumoxydgehalt bestimmt. Während des nichtthermischen Sinterns lassen sich zwei Bereiche unterscheiden: unterhalb von 900–1000 °C nimmt der Halsbereich aufgrund von Oberflächendiffusion stark zu, begleitet von geringer Verdichtung und Kornwachstum, während im Temperaturintervall von 900–1000 °C bis 1200 °C das Material eine Dichte von 95% der theoretischen Dichte erreicht. Dies wird durch Korngrenzendiffusion und beschleunigtes Kornwachstum verursacht. Dichtes Material mit einer Korngröße von 0.15–0.20 μm läßt sich durch isothermisches Sintern bei 1100–1150 °C herstellen.

In Y,Ce TZP segregiert das Yttrium bei 1150–1400 °C an den Korngrenzen. Bei den eingestellten experimentellen Bedingungen ist der Yttriumgehalt der Korngrenzen in Y,Ce-TZP unabhängig von der Temperatur und der Zeriumoxydkonzentration. Bei erhöhten Temperaturen (> 1200 °C) wird das Kornwachstum in dichtem TZP durch einen Lösungsmittragmechanismus bestimmt, dieser Eintrag ist am stärksten für Y-TZP, nicht vorhanden für Ce-TZP und mäßig für Y,Ce-TZP.

On présente étude de la croissance de grains et de la densification de polycristaux de zircone cérïée et yttriée (Y,Ce TZPs) par des traitements isothermes et non isothermes. On analyse les caractéristiques de Y,Ce TZPs en les comparant à celles de Y-TZP et Ce-TZP, ainsi que l'influence d'une augmentation de la concentration de cérium à concentration d'yttrium fixée. Dans le cas du frittage non isotherme on distingue deux régimes: en dessous de 900–1000 °C l'aire du col de frittage augmente nettement, par diffusion de surface accompagnée d'une densification et d'une croissance de grains très réduites, entre 900–1000 °C et 1200 °C les matériaux se densifient jusqu'à 95% de la densité théorique par diffusion aux

* To whom correspondence should be addressed

Journal of the European Ceramic Society 0955-2219/94/$7.00

joints de grains, tandis que la croissance des grains est accélérée. On peut préparer des matériaux denses avec des tailles de grains de 0·15–0·20 μm par frittage isotherme à 1100–1150°C.

Dans Y,Ce TZP c'est l'yttrium qui s'égrège aux joints de grains à 1150–1400°C. La teneur en yttrium des joints de grains dans Y,Ce TZP est indépendante de la température et de la teneur en cérium pour les cas étudiés. La croissance des grains dans TZP dense est contrôlée par un mécanisme d'entraînement du soluté à haute température (> 1200°C); ce phénomène d'entraînement se manifeste surtout dans Y-TZP, pas du tout dans Ce TZP et modérément dans Y,Ce TZP.

1 Introduction

Polycrystalline tetragonal zirconia ceramics represent a class of structural ceramics possessing high strength and toughness.[1] Their excellent mechanical properties are derived from the stress-induced martensitic transformation of the metastable tetragonal to the monoclinic phase.[2] In order to retain the tetragonal phase at room temperature the grain size must be kept below a critical value. This value depends, among other factors, on the concentration and type of oxide (e.g. Y_2O_3, CeO_2, MgO, CaO, etc.) used to stabilize the tetragonal phase, but is typically less than 1–3 μm. The most intensively studied systems are ZrO_2–Y_2O_3 and ZrO_2–CeO_2.

Yttria doped tetragonal zirconia polycrystals (Y-TZPs) possess a maximum bending strength equal to 1500 MPa at approximately 3 mol% Y_2O_3 (3Y-TZP) and a maximum in fracture toughness equal to 9–12 MPa $m^{1/2}$ at 2 mol% Y_2O_3.[3,4] In addition, it is well documented that grain growth in Y-TZP ceramics is extremely sluggish both under static and dynamic conditions.[5–9] Near theoretical densities with grain sizes in the submicron range can now routinely be obtained using commercially available powders. Fine-grained (0·3 μm) 3Y-TZP was the first ceramic material showing true superplastic behaviour, as demonstrated by Wakai *et al.*[10] in 1986. However, the main deficiency of Y-TZP materials is the poor stability of the tetragonal phase in humid atmospheres at 100–400°C.[11,12]

Ceria-doped tetragonal zirconia polycrystal (Ce-TZP) materials, on the other hand, display a considerably improved stability of the tetragonal phase[13] and possess a higher fracture toughness[1,14] compared to Y-TZP. However, grain sizes in Ce-TZP are generally in excess of 1 μm after free sintering[15] due to its high grain boundary mobility, making it *a priori* less attractive for hot forging processes. Indeed, no superplastic elongations have been obtained so far with Ce-TZP, due to strain hardening caused by extensive dynamic grain growth.[16] Finally, the bending strength of Ce-TZP is generally lower than that of Y-TZP materials.[1,14]

It is therefore anticipated that using both yttria and ceria as stabilizers for tetragonal zirconia will lead to a material with low grain boundary mobility, improved chemical stability and good mechanical properties. The improved stability of yttria–ceria stabilized tetragonal zirconia polycrystals (Y,Ce-TZPs) has indeed been reported by several authors[17–19] and is investigated in more detail elsewhere.[20] Limited work has been done so far on mechanical properties of Y,Ce-TZP, but the results seem promising. Hirano & Inada[21] reported a strength of 1000 MPa for 2·5 Y,4Ce TZP, while a toughness equal to 8 MPa $m^{1/2}$ is reported by the present authors elsewhere[20] for a similar composition. Preliminary work performed in this group[19] confirmed that Y,Ce-TZP has a much lower grain boundary mobility than Ce-TZP, especially at high temperatures (1400°C).

In this paper an analysis is presented of grain growth and densification of Y,Ce-TZP using both isothermal and non-isothermal techniques. The characteristics of Y,Ce-TZP are compared to those of Y-TZP and Ce-TZP and the effect of increasing ceria concentration at constant yttria concentration is evaluated. Segregation of solute cations to the grain boundaries has been analysed and the role of the segregated layer during grain growth is discussed. Segregation of solute cations to the grain boundaries and external surfaces has been observed in pure Y-TZP[6,22] and Ce-TZP doped with aliovalent elements.[23] This segregation layer is believed to hinder grain growth by means of a solute drag mechanism.[6] In pure Y-TZP yttrium segregates strongly to the free surfaces already at 1000°C,[22] while no segregation of cerium to the grain boundaries has been observed in 12Ce-TZP.[23]

An effort has been made to produce powders with good sinterability, which allow densification at low temperatures (1100–1500°C). In this way very fine-grained microstructures can be obtained, which are favourable among other factors, for superplastic forming processes, because of their enhanced ductility[24] and higher strain rates[25] compared to their coarser-grained counterparts.

2 Experimental Procedure

2.1 Powder synthesis

Zirconia powders with different amounts of yttrium and cerium (see Table 1) have been synthesized by a gel-precipitation technique using metal chlorides as precursor chemicals (hence the name 'chloride-method' to be used hereafter). The precursor

Table 1. Composition and theoretical densities of investigated powders

Code	ZrO_2 (mol%)	$YO_{1.5}$ (mol%)	CeO_2 (mol%)	ρ_{th} (g cm^{-3})
ZY5	95	5	-	6.06
ZY6Ce2	92	6	2	6.07
ZY4Ce2	94	4	2	6.09
ZY4Ce4	92	4	4	6.11
ZY4Ce6	90	4	6	6.14
ZY4Ce8	88	4	8	6.16
ZCe12	88	—	12	6.25

solution is added dropwise to an excess of a 25 wt% ammonia solution and the pH is maintained above 11. At this high pH the hydroxides of zirconium, yttrium and cerium precipitate instantaneously at high nucleation rates. In this way the different components mix on an atomic scale. The obtained gel is then thoroughly washed with water/ammonia mixtures to remove Cl^- ions. Hydrolysis and washing procedures were carried out in a baffled reactor vessel equipped with a dispersion or high energy disc turbine manufactured following the design of van de Graaf *et al.*[26] After the water/ammonia washing steps, the free water is removed by washing with ethanol. The replacement of water by ethanol lowers the capillary forces acting on the gel during drying significantly. Furthermore, ethoxy groups attach to the surface of the hydroxide particles and prevent to a large extent the formation of strong interparticle bonds during calcination.[27] The final product after calcination at 500–550 C is a nanocrystalline powder (crystallite sizes 8–10 nm) with a low degree of agglomeration. More experimental details concerning the synthesis method and powder properties can be found in Ref. 28. This synthesis method has been reported first by Haberko in 1979.[29] Van de Graaf *et al.*[26] designed a baffled vessel reactor especially suitable for this synthesis method.

2.2 Green compact formation and sintering

Green compacts were prepared by cold isostatic pressing of the synthesized powders, first at 100–200 MPa and finally at 400 MPa. Samples used for grain size analysis were heated during non-isothermal runs with 2 C/min in a Vectstar tube furnace (in air) to a temperature in the range 700–1400 C, immediately followed by cooling down. Isothermal experiments were conducted at 1100–1400 C for 2–15 h (heating/cooling rate 2 C/min). Disc shaped specimens (height 5–10 mm, diameter 10–15 mm) were used during non-isothermal experiments with maximum temperatures of 700–1150 C. All other experiments were performed with cylindrical specimens (height 11–18 mm, diameter 8–9 mm).

Free sintering behaviour has been analysed in detail by means of dilatometry using a Netzsch 402 E dilatometer. Densities were calculated from the green density and the observed linear shrinkage of the specimens, corrected for thermal expansion and weight loss (due to removal of absorbed water) of the specimens, using:

$$\rho(T,t) = \frac{(1 - [\Delta m/m_0])\rho_0}{\left\{1 - \left[\frac{(\Delta L/L_0)_{T,t} - \gamma\Delta T}{1 - \gamma\Delta T}\right]\right\}^3} \qquad (1)$$

where ρ_0 is the green density, $\Delta m/m_0$ the relative weight loss, $(\Delta L/L_0)_{T,t}$ the relative shrinkage at a given temperature T and time t, γ the thermal expansion coefficient and ΔT the temperature difference (with respect to room temperature). Good agreement was found between final densities calculated in this way with those measured by Archimedes' technique. During non isothermal experiments samples were heated with 2 C/min to 1450 C, while isothermal experiments were performed at 1100–1150 C for 15 h (heating rate 2 C/min, cooling rate 5 C/min).

2.3 Characterization of the porous texture

Nitrogen adsorption/desorption isotherms were obtained at 77 K using a Micromeritics ASAP 2400 system. Specific surface areas were analysed by the BET method. The *t* plot method[30] has been used to inspect if microporosity (pores having widths less than 2 nm) was present. Mesopore size distributions were calculated following the method developed by Barett *et al.* (the BJH method) assuming a cylindrical pore model.[31] Bulk densities were measured by Archimedes' technique (in Hg). Relative densities were calculated on the basis of the theoretical densities as listed in Table 1.

2.4 Grain size determination

Grain sizes (< 100 nm) were determined by X ray line broadening measurements using a Philips PW 1370 diffractometer with CuK_α radiation. For this purpose the specimens were ground after sintering and annealed at 800 C for 30 min in an attempt to remove residual stresses due to grinding. Step scans were taken over the range of 2Θ from 26 to 33 in steps of 0.015 (2Θ). At each step the intensity was measured during ten seconds. The specimen was rotated around the vertical axis to further improve counting statistics.

Three diffraction peaks appear in the measured 2Θ range: the (111) reflection of the tetragonal phase and the (-111) and (111) reflections of the monoclinic phase. The linewidths observed in this investigation caused an overlap of the two monoclinic reflections with the (111) reflection of the tetragonal phase, resulting in a poor resolution of the peaks even for

the samples heated to the highest temperature. A pattern-fitting technique based on the model developed by Schreiner & Jenkins[32] was therefore used to resolve the overlapping peaks. The grain size D was calculated from the pattern resolved (111) peak of the tetragonal phase using the Scherrer equation.

$$D_{(111)_t} = \frac{0{\cdot}94\,\lambda}{\beta_{1/2}\cos\theta} \qquad (2)$$

$\beta_{1/2}$ being the width of the peak at half maximum intensity corrected for the $K\alpha_1/K\alpha_2$ doublet and instrumental broadening, λ the wavelength of the radiation used (CuK_α) and Θ the Bragg angle.

Grain sizes <100 nm were determined by the lineal intercept technique from SEM micrographs (Hitachi S800 or Jeol JSM 35CF) of polished, thermally etched cuts using $D = 1{\cdot}56\,L$, where L is the average lineal intercept.[33]

2.5 X-Ray photoelectron spectroscopy (XPS)

The chemical composition of the grain boundaries has been analysed by means of XPS on intergranular fracture surfaces. Fracturing necessarily took place outside the UHV system of the XPS equipment. Measurements were performed using a Kratos XSAM 800 apparatus. Both MgK_α and AlK_α radiation have been used to generate photoelectrons. The Zr 3*d*, Y 3*d*, Ce 3*d* and Si 2*p* lines have been used for quantification. To correct for charging ($+3$–5 eV) the binding energy of the Zr $3d_{5/2}$ line has been fixed at 182·2 eV. More experimental details can be found elsewhere.[34,22]

3 Results

3.1 Non-isothermal experiments

3.1.1 Non isothermal grain growth and densification

Grain sizes during non-isothermal sintering up to 1150°C are shown in Fig. 1 as a function of temperature for three different Y,Ce-TZPs. The grain size evolution during non isothermal sintering of pure Y-TZP (composition ZY5·8) has been analysed by Theunissen *et al.*[9] and is also shown in Fig. 1 for reasons of comparison. All powders have an initial crystallite size of 8–9 nm (surface areas ranged from 95 to 125 m^2/g). The shape of the curves strongly suggest that two grain growth regimes can be distinguished. Up to 1000°C the grain size increases only very slowly to 20–30 nm, while above this temperature grain growth clearly accelerates.

The increase of density with temperature is shown in Fig. 2. Up to 1000°C the densities are very similar, above this temperature densification of ZY5·8 is somewhat faster. It can be seen that above 1000°C, where grain growth accelerates, relative densities of only 60% are observed. Upon heating from 1000 to 1200°C the density further increases to 95% for all compositions. The densification behaviour is analysed in more detail in Sections 3.1.3 and 3.2.1.

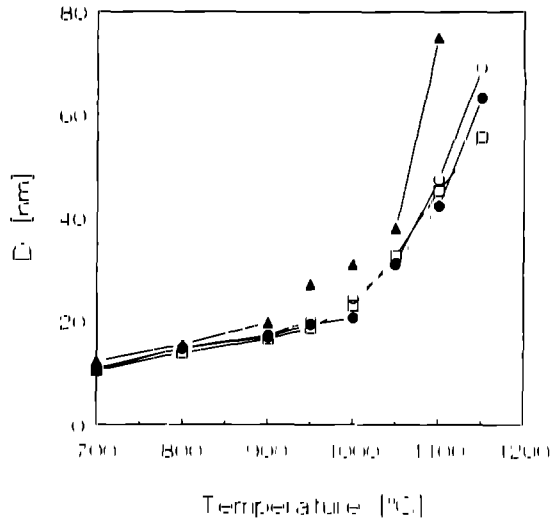

Fig. 1. Grain sizes, obtained by XRLB as a function of temperature during heating with 2°C/min. Data for ZY5·8 from Ref. 9 ●, ZY4Ce2, ○ ZY6Ce2; □, ZY4Ce4, ▲, ZY5·8.

Additional grain growth data during heating up to 1400°C are shown in Fig. 3 for ZY5 and ZY4Ce2. Above 1200°C the materials have essentially reached their final density (porosity is below 5%). It can be seen from Figs 1–3 that up to 1150°C both densification and grain growth are somewhat faster in Y-TZP than in Y,Ce-TZP. Above 1150–1200°C grain growth in pure Y-TZP is slower than in Y,Ce-TZP. These findings are further supported by isothermal experiments as described in Section 3.2.2.

Grain growth kinetics are normally analysed under isothermal conditions by measuring the grain size as a function of time, in accordance with classical grain growth theories as developed, amongst others, by Brook[35] for non-densifying

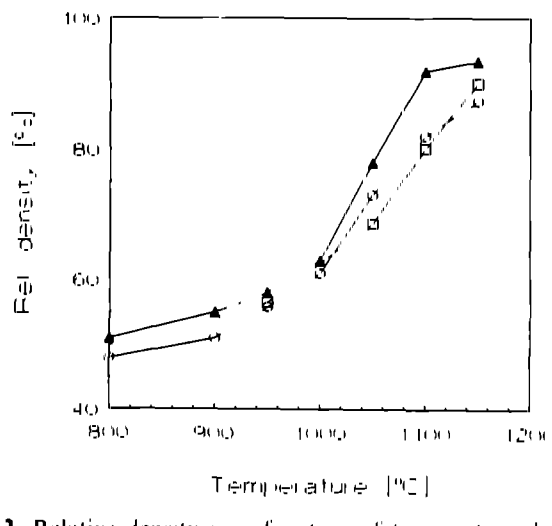

Fig. 2. Relative density as a function of temperature during heating with 2°C/min. Grain sizes in Fig. 1. ▲, ZY5·8; ○, ZY6Ce2; □, ZY4Ce4.

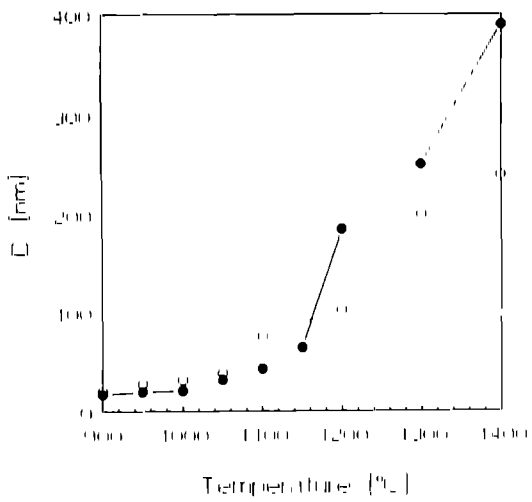

Fig. 3. Grain size as a function of temperature for ZY4Ce2 and ZY5.8 during heating with 2 °C/min. Note that at 1200 °C both materials are ≥ 95% dense. The data for the composition ZY5.8 were taken from Ref. 9. ●, ZY4Ce2; ○, ZY5.8.

systems. The general grain growth equation for isothermal conditions is:

$$D^n - D_0^n = kt \tag{3}$$

where D is the instantaneous grain size, D_0 the initial grain size in a particular grain growth regime, t time, k a kinetic constant and n is the so-called grain growth exponent. The grain growth exponent can have a value between 1 and 4 depending on the rate-limiting step during grain boundary migration.[35] Activation energies can be obtained from an Arrhenius plot with grain growth data recorded at a minimum of three temperatures. It can be shown (see the Appendix), that in the case of heating with a constant rate β the general grain growth equation transforms to:

$$D^n - D_0^n = \frac{K_1 RT}{\beta Q} \exp\left(-\frac{Q}{RT}\right) \tag{4}$$

where K_1 is a constant, the value of which depends on the rate limiting step during grain growth, Q is the apparent activation energy and RT has its usual meaning. Although eqns (3) and (4) are strictly speaking only valid for non densifying systems, it has been found by the present authors as well as by others[9, 36] that even in highly porous systems grain growth can be adequately described by these equations. It is clear, however, that the apparent activation energy cannot be attributed to grain boundary migration only, but must certainly be influenced by the densification process.

Equation (4) can be rearranged to:

$$\ln(D^n - D_0^n) - \ln(T) = \ln\left(\frac{K_1 R}{\beta Q}\right) - \frac{Q}{RT} \tag{5}$$

By plotting the left hand side of eqn (5) versus $(1/T)$ a straight line should be obtained, the slope being equal to $(-Q/R)$. Linear regression by the least squares method using eqn (5) has been performed to determine which n value provides the best fit. The value of the apparent activation energy is calculated from the slope of the best-fit curve.

At temperatures below 1000 °C the best fit is obtained for a n value of 3 to 4, the difference in correlation coefficient being too small to allow further discrimination. The corresponding activation energies are rather low and are typically equal to 90 ± 16 kJ/mol ($n = 3$) and 130 ± 34 kJ/mol ($n = 4$) for all compositions. The differences in correlation coefficients of the different n values are rather small in the temperature range 1000–1150 °C, but the data are best represented by $n = 2$–3. The apparent activation energies are typically 295 ± 65 kJ/mol ($n = 2$) and 375 ± 80 kJ/mol ($n = 3$) for the investigated Y,Ce-TZPs.

3.1.2 Porous textural evolution during non isothermal sintering

It has already been shown that densification and grain growth of the different Y,Ce-TZPs is quite similar up to 1000 °C. Therefore, the porous textural evolution of only one composition (ZY6Ce2) has been studied. In Fig. 4 the nitrogen adsorption/desorption isotherms of a green compact and of compacts heated to 800 and 1000 °C respectively are shown. All the isotherms are of type IV according to the BDDT (Brunauer, Deming, Demming and Teller) classification,[37] which is characteristic of mesoporous systems. The shape of the hystereses gradually changes from type E to type A, following the classification of de Boer.[38] This indicates[38] that the pore shape changes from tubular capillaries with wide parts of various widths in the green compact to purely cylindrical at 1000 °C. Figure 5 shows a t plot of the green compact, where the adsorbed volume (STP) is plotted versus the statistical thickness of the adsorbed multilayer. This t plot has been constructed from the adsorption isotherm of the green compact given in Fig. 4 using

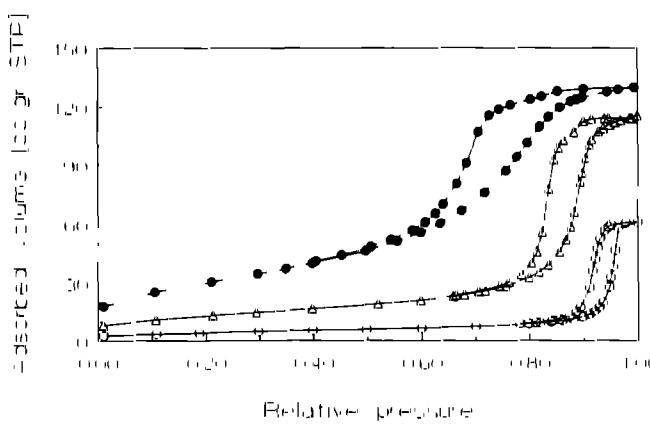

Fig. 4. N_2 sorption isotherms of ZY6Ce2 compacts, in the green state (●) and after heating with 2 °C/min to (△) 800 and (○) 1000 °C.

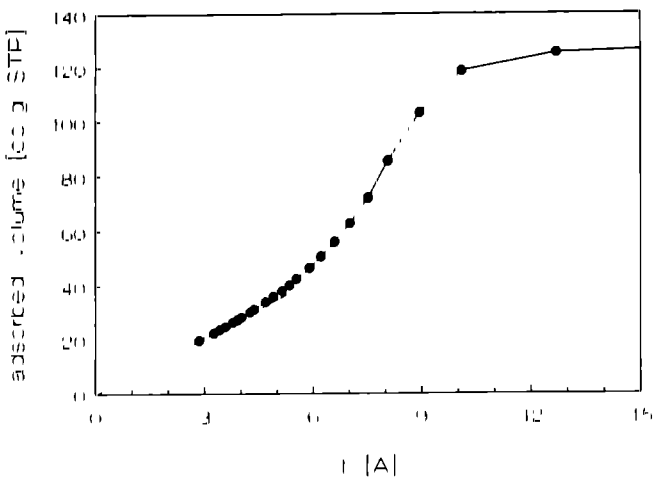

Fig. 5. Representative t plot of a green compact of ZY6Ce2, as calculated from the adsorption isotherm shown in Fig. 4

the appropriate standard isotherm of a non-porous solid given by Lecloux & Pirard.[39] The standard isotherm is selected taking into account the C_{BET} value (= 107 in the case of ZY6Ce2 in the green state) and consequently the adsorbate–adsorbent interaction. The shape of the *t*-plot of Fig. 5 is representative of a mesoporous solid showing filling of pores due to capillary condensation. The linear branch of the *t*-plot goes through zero, demonstrating the absence of microporosity. The surface area (S_t) calculated from the slope of the linear branch of the *t*-plot[39] is identical to the BET surface area. No microporosity corrections of the S_{BET} values are therefore necessary. Figure 6 shows the pore size distributions (PSDs)—as calculated from the adsorption branch—for a green compact and after heating to 800–900°C. It is clear that the PSD is becoming sharper and the pores are coarsening during sintering; the most frequently observed pore radius increases from 4·4 nm in the green compact to 13·5 nm after heating to 900°C. Pore sizes calculated from the adsorption branch of the hysteresis are representative of the 'wide bodies' of the pores, while pore sizes calculated from the desorption branch represent the pores' entrances. PSDs calculated from the desorption branch are generally sharper and are often used in ceramic technology, but the 'wide bodies' determine the sinterability of a material.

Normally, grain growth is considered to occur only in the last stage of sintering, where porosity is less than 10%. This investigation as well as those of others[36,40] has shown that grain growth occurs at high values of porosity. In the low temperature (LT) regime, i.e. below 1000°C, the porosity is decreasing from 55% in the green compact to 35–40% at 1000°C. To have a better understanding of grain growth in such porous materials, one would like to know how the amount of neck area (and thus the amount of solid–solid interface) increases with temperature. For this purpose the fraction of the geometrical surface area (S_{GEO}), which is not accessible to nitrogen $\{(S_{GEO} - S_{BET})/S_{GEO}\}$ is calculated. The geometrical surface area can be calculated from the crystallite sizes determined from XRLB assuming (i) the crystallites have spherical morphology and (ii) no closed porosity is present.[41] With these assumptions $\{(S_{GEO} - S_{BET})/S_{GEO}\}$ is identical with the total (fractional) neck area per grain S_{NECK}/S_{GEO}. The neck area has been found to increase with temperature from 30% at 800°C to 90% at 1100°C. At that stage the density equals 80–85% in Y, Ce-TZP and some closed porosity is present. The fractional neck area is therefore in reality somewhat lower than 90% at 1100°C.

To identify the relative importance of neck growth and densification during sintering, $\{(S_{GEO} - S_{BET})/S_{GEO}\}$ is plotted as a function of relative density in Fig. 7. The variation of the specific surface area alone with density is also shown in this diagram. Clearly, two regimes can again be distinguished: a steep increase of the neck area with only very little densification followed by a strong increase of relative density accompanied by further moderate

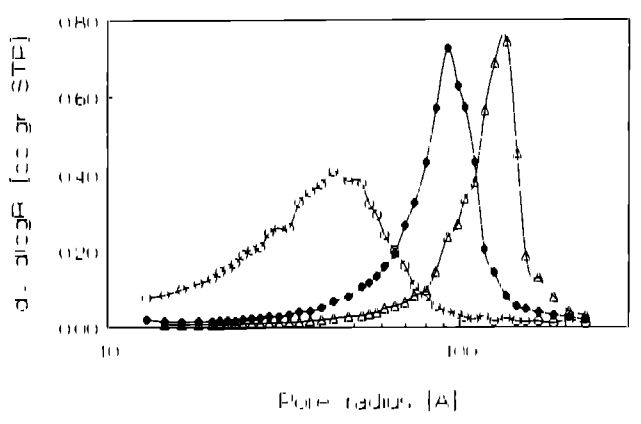

Fig. 6. Pore size distributions of ZY6Ce2 in the green state (○) and after heating to (◆) 800 and (△) 900°C, as calculated from the adsorption branch of N_2 sorption isotherms

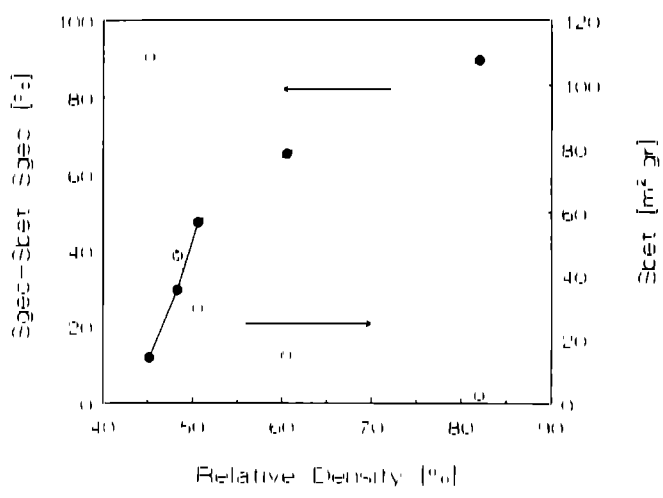

Fig. 7. The fraction of the geometrical surface area not accessible to N_2 (●), respectively the BET surface area (○) versus relative density.

neck growth. The transition temperature is situated between 900 and 1000°C. This diagram is considered to be strong evidence that surface diffusion is the dominant mass transport below 900–1000 °C in these nanostructured materials.

3.1.3 Kinetic analysis of non isothermal sintering

In the remaining part of the analysis presented here attention will be focused on the composition series ZY4Ce$_x$ with x = 2–8 mol%, in order to evaluate the effect of increasing ceria concentration at constant yttria content. The sintering kinetics of the end members of this composition series (x = 2 and 8) have been analysed on the basis of initial stage sintering models.

The general equation for isothermal initial stage sintering is[42]

$$\frac{\mathrm{d}}{\mathrm{d}t}(\Delta L/L_0) = K_0 \exp\left(-\frac{Q}{RT}\right)(\Delta L/L_0)^m \qquad (6)$$

where $\Delta L/L_0$ is relative shrinkage, t is time, K_0 a numerical constant, m the sintering exponent and the other symbols have their usual meaning. Values of K_0 and m have been tabulated for different sintering mechanisms and geometries.[42] For a two-sphere geometry $m \approx 1$ in the case of volume diffusion and $m \approx 2$ in the case of grain boundary diffusion.

Young & Cutler[43] have shown that in the case of heating with a constant rate eqn (6) can be reformulated into an integral form as follows

$$(\Delta L/L_0)/T = K_1 \exp\left[-\frac{Q}{(m+1)RT}\right] \qquad (7)$$

where K_1 is a numerical constant and the other symbols have the same meaning as previously defined. It follows from eqn (7) that the slope of a plot of $\ln\{(\Delta L/L_0)/T\}$ versus $(1/T)$ is equal to $(-Q/(m+1)R)$. The value for the apparent activation energy can then be calculated assuming a certain sintering mechanism with its characteristic m value to be dominant. Alternatively, m can be determined using either isothermal or non isothermal techniques as will be demonstrated now.

Integration of eqn (6) leads to

$$(\Delta L/L_0)^{m+1} = K_0 \exp\left(-\frac{Q}{RT}\right)t \qquad (8)$$

By analysing the time dependence of the relative shrinkage under isothermal conditions one can thus determine the m value. Alternatively, m can be determined by performing experiments with different constant heating rates (CHR). It has been shown by Woolfrey & Bannister[44] that for CHR experiments the following relation holds between the relative shrinkage at a particular temperature $(\Delta L/L_0)_T$ and the heating rate β:

$$\ln(\Delta L/L_0)_T = -\frac{\ln \beta}{(m+1)} + \ln K_2 \qquad (9)$$

where K_2 is a numerical constant. Equation (9) shows that a double logarithmic plot of relative shrinkage at a specific temperature versus heating rate gives a straight line of slope $\{-1/(m+1)\}$. All the techniques mentioned above have been applied to analyse the sintering behaviour of Y,Ce TZP.

In Fig. 8 $\ln\{(\Delta L/L_0)/T\}$ has been plotted versus $(1/T)$ during heating with 2°C/min for ZY4Ce2. The increase in relative density with $(1/T)$ is also shown in this figure. The corresponding diagram of ZY4Ce8 is very similar to the one shown in Fig. 8. For both compositions two linear parts can be recognized, one at low and one at high temperatures. Two parallel-concurrent mechanisms are seen to operate. The low temperature (LT) mechanism is dominant between 600–800 °C, while the high temperature (HT) mechanism is dominant above 900 °C. At temperatures above 1150–1170 °C the curves deviate strongly from linearity, because the assumptions underlying eqns (5)–(6) are no longer valid at the observed shrinkage values.

From an isothermal sintering experiment conducted at 1045 °C with ZY4Ce8 it has been determined that m equals 3.5 ± 0.1 using eqn (7) for relative shrinkages of 8·5–15%. This shrinkage interval is, in fact, partly situated in the second stage of sintering. The high sinterability of the investigated TZPs makes it quite difficult to characterize the first stage of sintering during isothermal experiments at temperatures of 1000 °C or more, even at very high heating rates. CHR experiments with heating rates of 2, 10 and 20 °C/min have therefore also been performed with this composition and in Fig. 9 relative shrinkages at 920–1040 °C (1·3–7·4%) are

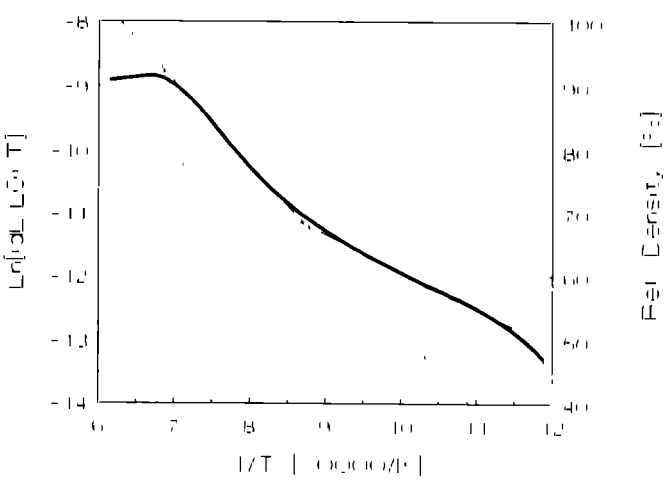

Fig. 8. The relative density ( ), respectively the natural logarithm of $[(\Delta L/L_0)/T]$ (——) versus the inverse of temperature during heating with 2°C/min of ZY4Ce2, as measured by dilatometry.

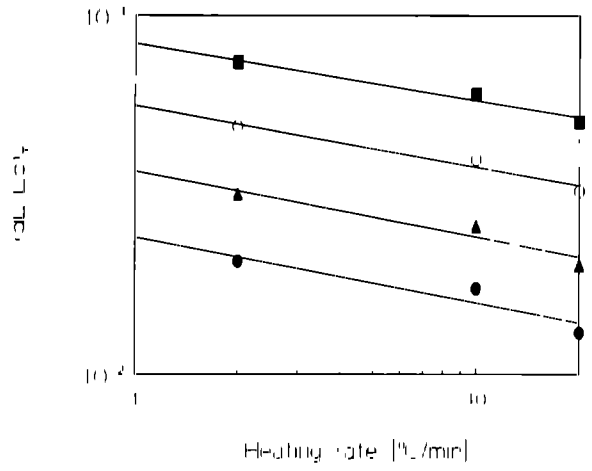

Fig. 9. The relative shrinkage of ZY4Ce8 at a particular temperature $(\Delta L/L_0)_T$ versus heating rate, as measured by dilatometry for heating rates of 2, 10 and 20 °C/min ●, 920 °C, ▲, 960 °C, ○, 1000 °C ■ 1040 °C

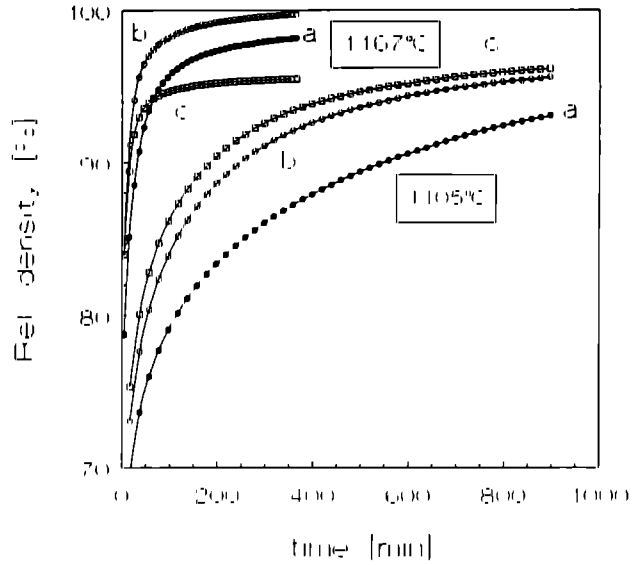

Fig. 10. Relative density as a function of time during free sintering at 1105 and 1167 °C of (a) ZY5, (b) ZY4Ce8 and (c) ZY4Ce2. Heating rate 2 °C/min, measured by dilatometry

plotted versus heating rate double logarithmically. An average m value of 4·7 ± 1·7 has been determined from the slope of these plots using eqn (9). The m value determined from the isothermal experiment (3·5) is within the 68% confidence interval of the CHR value. The m values determined here (3·5–4·7) are considerably higher than the ones predicted from grain boundary ($m \approx 2$) and volume diffusion ($m \approx 1$) two-sphere models. A possible explanation for these high m values will be given in Section 4.

An m value of 4 has been taken as typical for the HT sintering regime. Due to the very small shrinkages (0·1–1·1%) observed in the LT regime it has been found impossible to determine its characteristic m value. Consequently, the apparent activation energy for densification can only be calculated from the slope of the linear part of the curve shown in Fig. 8 belonging to the HT mechanism. The activation energies (using $m = 4$) are 540 kJ/mol and 655 kJ/mol for ZY4Ce2 and ZY4Ce8 respectively. These results are in good agreement with the results of Wang & Raj,[45] who determined Q to be equal to 615 ± 80 kJ/mol for 2·8 Y-TZP.

3.2 Isothermal experiments

3.2.1 Isothermal sintering

In this section the minimum temperature required to obtain densities ≥95% with the different investigated compositions is sought. This temperature should preferably be below 1200 °C to obtain very fine-grained microstructures, since grain growth in Y,Ce-TZP accelerates above this temperature, as has been shown in Fig. 3. In Fig. 10 the increase in relative density with time at 1105 and 1167 °C is shown for three compositions: ZY5, ZY4Ce2 and ZY4Ce8. At 1105 °C densification proceeds slowly; after 15 h 95–96% is reached for the Y,Ce-TZPs and 92% for ZY5. At 1167 °C densification is much faster and densities near 95% are obtained after only 200 min for all three compositions. Separate sintering experiments performed in a tube furnace at 1100–1150 °C confirmed the results obtained with the dilatometer and showed very little difference in end densities for the four investigated ZY4Ce$_x$ (x = 2–8) compositions. At 1100 °C the final density of ZY5 is generally lower than those of ZY4Ce$_x$, at 1150 °C all densities are quite similar. Sintering experiments performed with other powder batches, having the same chemical composition as studied here, show that the sintering results presented in Fig. 10 are reproducible. Grain sizes after isothermal sintering are reported in Section 3.2.2.

Based on the authors' experience with different batches of ZY5, ZY4Ce$_x$ and also ZCe12, it can be concluded that the sintering behaviour at such low temperatures (1100–1150 °C) of the nanostructured powders produced by the chloride method is controlled predominantly by the degree of agglomeration and to a much lesser extent by the composition, provided no exaggerated grain growth occurs, as for instance in ZCe9.[19]

3.2.2 Isothermal grain growth

By low-temperature sintering—as described in the previous section—the authors have tried to limit grain growth. The minimum temperature to reach ±95% relative density has been found equal to 1100 °C for Y,Ce-TZP, the minimum attainable grain size being equal to 0·15 μm (reached after 200 min at this temperature) for these materials. Figure 11 shows this microstructure for ZY4Ce2.

Grain sizes after isothermal heat treatment at 1150–1400 °C are given in Table 2 for ZY5, ZY4Ce$_x$ and ZCe12. All samples had densities of 95–99%. It can be seen that after 1150 °C/10 h all compositions have an identical grain size (0·2 μm). At higher

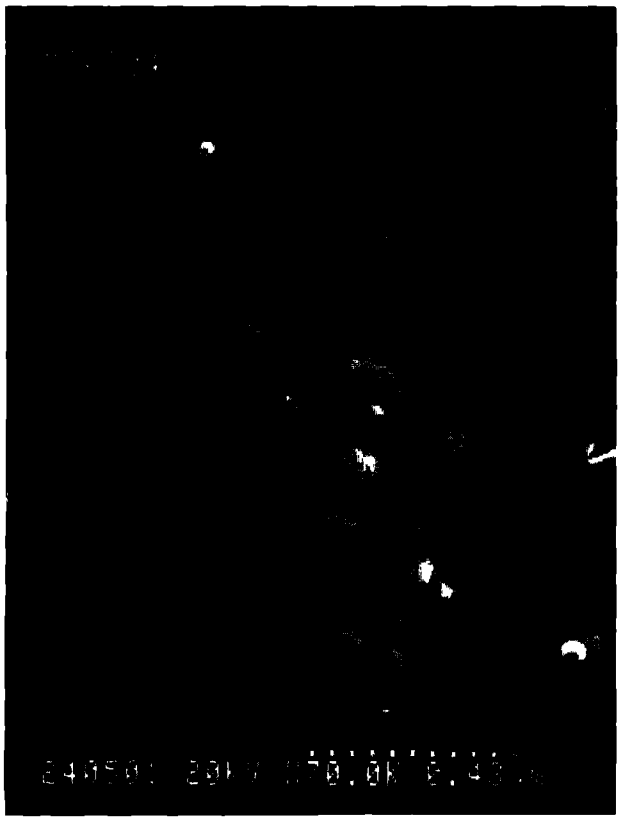

Fig 11. SEM micrograph of ZY4Ce2 sintered at 1100 C during 200 min

temperatures, however, the differences in grain growth rates become appreciable. At 1400 C grain sizes in ZCe12 are in the micron range, while the grain size in ZY5 after 1400 C/3 h remains only 0.3 μm, grain sizes of Y,Ce-TZP are intermediate between ZY5 and ZCe12, but still in the submicron range. Increasing the ceria concentration in ZY4Cex (with x = 2–8) does not affect grain growth within the investigated concentration and temperature range.

3.3 Grain boundary segregation

It has been demonstrated in the previous section that grain growth of Y,Ce-TZP at 1400 C is intermediate between Y-TZP and Ce-TZP, the largest grain sizes being observed for 12Ce-TZP. At much lower temperatures, i.e. 1150 C, no appreciable differences were found. Therefore the segregation of yttrium and cerium to the grain boundaries has been analysed with XPS after heat treatments in air at 1150 C (10 h) and 1400 C (3 h). The possible presence of silicon at the grain boundaries has also been examined.

Table 3. Composition of the grain boundary region as analysed by XPS

Bulk composition	*Grain boundary composition*	
	1150 C/10 h	*1400 C/3 h*
ZY5	ZY11.2	ZY9.1
ZY4Ce2	ZY9.2Ce3.6	ZY7.9Ce3.2
ZY4Ce4	ZY7.6Ce3.5	ZY7.8Ce2.7
ZY4Ce6	ZY7.4Ce5.2	ZY7.5Ce7.3
ZY4Ce8	ZY6.1Ce7.0	ZY6.9Ce9.1

The composition of the grain boundary regions as determined by XPS are given in Table 3 for ZY5 and ZY4Cex (x = 2–8) at 1150 C and 1400 C. The information depths in the XPS analysis are 5–6 nm, for Zr, Y and O and 3 nm for Ce. In Y,Ce-TZP very little segregation of cerium has been observed, while yttrium was enriched by a factor of $\sim$ 2 with respect to the bulk composition at both temperatures. Table 3 also shows that the yttrium enrichment of the grain boundaries in ZY5, as studied by XPS, is slightly higher in this material than in ZY4Cex. Grain boundaries in ZY5 have been analysed in greater detail with XPS, SAM and TEM and the results are fully described in Ref. 34. The most important observations are that after sintering at 1150 C a continuous film of an amorphous silicate phase with a thickness $\geq$ 10 Å is present at the grain boundaries (TEM) and that the Y/Zr ratio in the first 1–2 nm is as high as 0.3 (SAM). In Y,Ce-TZP no silicon could be detected with XPS.

In oxides the most important driving forces for segregation of solute cations to the free surfaces or grain boundaries are (i) strain energy relaxation and (ii) electrostatic charge compensation.[46] The strain energy arises from the size mismatch between the solute and host cation. The ionic radii[47] and misfit values ε ($= (R_A - R_B)/R_B$, where R_A is the ionic radius of the solute cation and R_B the ionic radius of Zr^{4+}) of the cations present in the zirconia ceramics studied here are given in Table 4. As can be seen in this table, the misfit increases in the order Ce^{4+}, Y^{3+}, Ce^{3+}. It is well documented[22] that cerium can

Table 2. Grain sizes (μm) after isothermal heat treatments

Composition	*1150 C/10 h*	*1200 C/20 h*	*1400 C/3 h*
ZY5	0.20	0.21	0.30
ZY4Ce2	0.21	0.23	0.62
ZY4Ce4	0.21	n.d.	0.62
ZY4Ce6	0.21	n.d.	0.61
ZY4Ce8	0.22	0.24	0.66
ZCe12	0.23	0.38	$\sim$ 1.0

n.d. Not determined

Table 4. Ionic radii and misfit values of the cations present in the studied zirconia ceramics

Ion	*Ionic radius*[a] (Å)	*Misfit* ε
Zr^{4+}	0.84	-
Y^{3+}	1.019	0.21
Ce^{4+}	0.97	0.16
Ce^{3+}	1.143	0.36

[a] Taken from Ref. 47

Table 5. Binding energies (BE) of the photoelectron lines in the Ce 3*d* region 48, when cerium is in a mixed oxidation state

Ion	*BE* $3d_{5/2}$ (*eV*)	*BE* $3d_{3/2}$ (*eV*)	*Remark*
Ce^{4+}	882.1	900.6	Main lines
	888.4	907.1	Satellites
	898.1	916.5	Satellites
Ce^{3+}	880.9	899.7	Main lines
	885.3	903.8	Satellites

be in the trivalent state after sintering in air at elevated temperatures. A large driving force for segregation is expected for trivalent cerium because of the considerable size mismatch (Table 4) and the charge difference between Ce^{3+} and Zr^{4+}. Therefore, the oxidation state of cerium in YCe-TZP has been studied by means of XPS. For this purpose, the Ce 3*d* spectra of ZY4Ce2 and ZY4Ce8 have been recorded after sintering in air at 1150 and 1400 °C.

The binding energies (BEs) of the main and satellite lines in the Ce 3*d* region have recently been reported for CeO_2 and Ce_2O_3 by Paparazzo *et al.*[48] and are given in Table 5. The presence of two shake-up satellite pairs of the Ce 3d doublet for Ce^{4+} and one shake-up satellite pair for Ce^{3+} with intensities approaching those of the main lines makes the quantitative analysis of the fraction of trivalent cerium quite complicated. Nevertheless, an attempt has been made to determine this fraction by deconvolution of the Ce 3*d* region, yielding the contributions of the photoelectron lines of Ce^{4+} and Ce^{3+} to the observed intensity profile.

Only in the case of ZY4Ce8 was the signal-to-noise ratio sufficient to allow deconvolution of the Ce 3*d* region. Deconvolution has been performed with the software package supplied by Kratos to the Kratos XSAM-800 apparatus. The following procedure has been used: (i) Gaussian line profiles were assumed, (ii) the binding energies of Table 5 were used as starting values and a BE interval of 1 eV, centred around the BEs of Table 5 for each line, was allowed during minimization, (iii) the upper limit of the full width at half maximum (FWHM) was set at 4 eV for each line and (iv) the FWHM of each line belonging to either Ce^{4+} and Ce^{3+} should have the same value.

Deconvolution of the Ce 3*d* region performed in this way demonstrated that the fraction of trivalent cerium at the grain boundaries of YCe-TZP equals approximately 50–55% independent of temperature. Figure 12 shows the Ce 3*d* spectrum of the fracture surface of ZY4Ce8 after deconvolution, the various photoelectron peaks of both cerium species are indicated.

Since (i) no effect of increasing ceria concentration on grain growth in ZY4Ce*x* has been observed and (ii) the grain boundaries are not enriched in cerium, but show identical enrichment in yttrium, it is concluded that the migration of the segregation layer of yttrium along with the moving grain boundary is the rate-limiting step during grain growth in Y,Ce-TZP. This point is further elaborated in Section 4.

4 Discussion

4.1 Sintering and concurrent grain growth

During heating with 2 °C/min final densities $\geq 95\%$ are obtained at 1200 °C with all investigated compositions. Below this temperature densification and grain growth are occurring simultaneously. Two regimes can be distinguished here (Section 3.1) a LT regime at temperatures below 900–1000 °C and a HT regime between 900–1000 and 1200 °C. In the LT regime only a very limited grain growth and densification is observed, but important structural changes are nevertheless taking place. The neck area increases strongly from 12% in the green compact to 50–65% at 900–1000 °C (see Fig. 7). Simultaneously, pore coarsening is taking place. Since the neck area increases strongly with only little densification surface diffusion is the dominant mass transport mechanism (evaporation–condensation processes are very unlikely at these low temperatures). In a two sphere model no densification can occur with surface diffusion. Lange,[49] however, proposed recently that in real powder compacts some densific

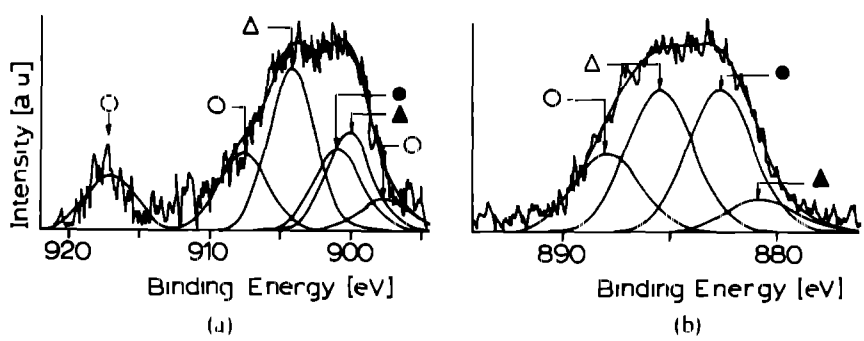

Fig. 12. Deconvoluted Ce 3*d* spectrum measured on the fracture surface of ZY4Ce8 (annealed at 1400 °C). ▲,●, main lines ($Ce\,3d_{5/2}$ and $Ce\,3d_{3/2}$), △,○ satellite lines, ▲,△, Ce^{3+}, ●,○, Ce^{4+}

ation may occur if diffusion distances are short, as in the nanostructured materials studied here. Below 1000°C a grain growth exponent $n = 3$–4 best fitted the data for all investigated compositions. Greskovich & Lay[36] reported similar grain growth kinetics in very porous alumina compacts at 1470 C. They indicated that if surface diffusion predominates and grain boundary migration is rapid compared to neck growth, a grain growth law with $n = 3$ is obeyed. Such a grain growth mechanism could well be operating in the LT regime in the TZPs studied here, considering the observed n values (3–4) and the fact that surface diffusion was found to be the dominant mass transport mechanism.

In the HT regime (1000–1200 C) grain growth and densification accelerate clearly (see Figs 1 and 2). Grain growth in Y TZP is slightly faster than in Y,Ce TZP, but this must be correlated with the faster densification of Y TZP leading to a larger fraction of solid–solid interfaces. Undisturbed grain growth ($n = 2$) is most likely occurring at this stage. Considering the relatively low temperatures (900–1150 C) of this densification regime and the very fine particle size (< 100 nm), grain boundary diffusion is considered to be the dominant mass transport mechanism. Analysis of the sintering kinetics of Y,Ce TZP in this regime (Section 3.1.3) showed that the time-dependence of relative shrinkage was much weaker (i.e. high m values) than expected on the basis of grain boundary (and volume) diffusion two sphere models (see Section 3.1.3). A similar time dependence as observed here has been reported by Duran *et al.*,[30] who performed isothermal sintering experiments at 960–1065 C with Er-TZP. This weak time dependence is most likely due to reorganization of the particle stacking, induced by local particle coordination fluctuations as explained by Veringa.[31] This leads to opening of larger pores and microcracks (if the amplitude of the fluctuations is larger than a critical value), which are only slowly removed during progressive sintering.

It is interesting to note that the microstructure development of nanostructured titania during non-isothermal sintering is quite similar to that of zirconia reported here. Hahn *et al.*[32] also observed two regimes in TiO_2: below 900 C grain growth proceeds very slowly and surface diffusion is the dominant mass transport mechanism, above 900 C grain growth is very fast.

4.2 Grain growth in the dense state, relation with solute drag

As already illustrated, grain growth during sintering is influenced significantly by the densification process itself. Differences in grain boundary mobilities with composition are thus easier to recognize in non densifying systems as described in Section 3.2.2. It has been found that the differences in grain growth of Y TZP, Ce TZP and Y,Ce-TZP are insignificant at 1150 C and only become important at higher temperatures ($\geq$ 1200 C). At 1400 C Ce-TZP clearly has the highest grain boundary mobility, Y TZP the lowest and Y,Ce-TZP is intermediate between these two.

Winnubst *et al.*[6] were the first to suggest that grain growth in ZrO_2–Y_2O_3 is controlled by a solute drag mechanism. In Section 3.3 it has been shown that both in Y TZP and Y,Ce-TZP it is yttrium that segregates to the grain boundaries with the highest segregation levels observed in Y TZP. This is in good agreement with the XPS analysis of Theunissen *et al.*[33] of segregation to the free surfaces of Y TZP and Y,Ce TZP. It has furthermore been observed that the level of yttrium segregation was not very sensitive to temperature in the investigated range (1150–1400 C), the Y/Zr atomic ratio being equal to $\sim$0.1 (enrichment factor $\sim$ 2) at the grain boundaries as measured by XPS. SAM measurements gave an Y/Zr atomic ratio of $\sim$0.3 (enrichment factor $\sim$ 6).[34] It can now be calculated that the information depth of the SAM analysis is equal to the thickness of the segregation layer, while the XPS analysis has an information depth that extends into the bulk of the grains with nominal chemical composition. For a full discussion of yttrium segregation in Y TZP the reader is referred to Ref. 34. As mentioned before no segregation of cerium to the grain boundaries has been observed in 12Ce TZP.[23]

In section 3.3 it has been demonstrated that 50–55% of the cerium cations are in the trivalent state at the grain boundaries of YCe TZP after sintering in air at 1150–1400 C. The misfit for Ce^{3+} in zirconia is quite high (see Table 4), but no significant segregation of cerium has been observed. The reduction of Ce^{4+} to Ce^{3+} in ceria during heat treatments in air takes place at temperatures below 1400 C only if traces of silica are present.[35] Therefore, it is anticipated that cerium is only trivalent at the grain boundaries of YCe TZP where silica is present (be it in concentrations below the detection limit of XPS) and remains in its highest oxidation state in the grain interior. This is supported by the impedance analysis of Y TZP and YCe TZP (sintered in air) performed by Hernandez *et al.*,[24] who observed that the bulk conductivity of Y TZP did not increase when codoping with ceria. Such an increase of the bulk conductivity should have been observed if cerium was trivalent in the grain interior of an ionic conductor like Y TZP, since this would have led to an increase of the oxygen vacancy concentration according to

$$2Ce'_{Zr} + O_O^x \rightarrow 2Ce'_{Zr} + V_O^{\cdot\cdot} + \tfrac{1}{2}O_2\uparrow$$

Although differences in segregation of the stabilizers are quite significant comparing Y-TZP, Y,Ce-TZP and Ce-TZP, differences in grain growth only appear clearly at 1400°C. Examination of the microstructures after 1150°C/10 h, showed no evidence for pinning of the grain boundaries by residual pores. It is therefore proposed that at 1150°C, being a very low temperature for grain growth in dense TZP, grain boundary velocities are so low, that the segregation layer exerts no drag on the moving boundary. At higher temperatures the grain boundary velocity increases and the segregated layer starts exerting a drag on the boundary. This drag is maximum in Y-TZP, absent in Ce-TZP and intermediate between these in two in Y,Ce-TZP, explaining the differences in grain growth observed at higher temperatures.

5 Conclusions

(a) Nanostructured Y-TZP and Y,Ce-TZP powders produced by the chloride-method can be pressureless densified at low temperatures (1100–1150°C) to densities $\geq 95\%$ with average grain sizes of 0.15–0.20 μm.

(b) During non-isothermal sintering of these materials two regimes are distinguished: one below 900–1000°C, in which the neck area increases strongly with only little densification and one at temperatures from 900–1000 to 1200°C, where the largest part of densification occurs. At low temperatures surface diffusion is the dominant mass transport mechanism. Above 1000°C densification occurs most likely via grain boundary diffusion and is retarded by reorganization processes.

(c) Grain growth during non-isothermal sintering can be similarly divided into two regimes. Below 900–1000°C neck formation via the surface diffusion is rate limiting ($n = 3$), while above this temperature the neck area has increased to $\sim 60\%$ and undisturbed grain growth ($n = 2$) occurs for all investigated compositions.

(d) Segregation of yttrium to the grain boundaries is observed at 1150–1400°C in both Y-TZP and Y,Ce-TZP, the highest segregation levels being observed for Y-TZP. No significant segregation of cerium has been found in Y,Ce-TZP. In Y-TZP the enrichment factor equals ± 6 in the first 1–2 nm of the grain boundary region as found by SAM.

(e) Normal grain growth occurs at 1150–1200°C in dense TZP and very little differences with composition are observed. At higher temperatures grain growth is controlled by a solute drag mechanism. This drag is highest for Y-TZP, absent for 12Ce-TZP and moderate for Y,Ce-TZP. Increasing the ceria concentration at constant yttria content has no effect on grain growth and yttria segregation within the investigated composition series (ZY4Cex, with x = 2–8).

Acknowledgements

Akzo Chemicals b.v. is gratefully acknowledged for financial support of this investigation. René Olde Scholtenhuis is acknowledged for performing part of the powder synthesis and sample preparation, Theo Leuwerink for performing physisorption and mercury penetration measurements, Joop Snoeyenbos for machining and polishing, Jaap Boeijsma for his assistance with XRD measurements, Marc Smithers for SEM observations and Albert van den Berg for recording the XPS spectra.

References

1 Swain, M. V. & Rose, L. R., Strength limitations of transformation toughened zirconia alloys. *J. Am. Ceram. Soc.*, **69**(7) (1986) 511–18.

2 Green, D. J., Hannink, R. H. J. & Swain, M. V., *Transformation Toughening of Ceramics*. CRC Press, Boca Raton, Florida, 1989, pp. 64–84.

3 Tsukuma, K., Kubota, Y. & Tsukidate, T., Thermal and mechanical properties of Y_2O_3 stabilized tetragonal zirconia polycrystals. In *Advances in Ceramics*, Vol. 12, 1984, pp. 382–90.

4 Wang, J., Rainforth, W. M. & Stevens, R., The grain size dependence of the mechanical properties in TZP ceramics. *J. Eur. Ceram. Soc.*, **10** (1992) 21–31.

5 Lange, F. F., Transformation toughened ZrO_2 correlations between grain size control and composition in the system ZrO_2–Y_2O_3. *J. Am. Ceram. Soc.*, **69**(3) (1986) 240–2.

6 Winnubst, A. J. A., Theunissen, G. S. A. M., Groot Zevert, W. F. M. & Burggraaf, A. J., The sintering behaviour of fine grained ZrO_2–Y_2O_3 ceramics. In *Science of Ceramics*, Vol. 14, 1987, pp. 309–14.

7 Nieh, T. G. & Wadsworth, J., Dynamic grain growth during superplastic deformation of yttria stabilized tetragonal zirconia polycrystal. *J. Am. Ceram. Soc.*, **72**(8) (1989) 1469–72.

8 Nauer, M. & Carry, C., Grain growth in yttria doped tetragonal zirconia polycrystals (Y-TZP). In *Proceedings of the International Conference on Grain Growth in Polycrystalline Materials*, Rome, 1991, to be published.

9 Theunissen, G. S. A. M., Winnubst, A. J. A. & Burggraaf, A. J., Sintering kinetics and microstructure development of nanoscale Y-TZP ceramics. *J. Eur. Ceram. Soc.* **11** (1993) 315–24.

10 Wakai, F., Sakaguchi, S. & Matsuno, Y., Superplasticity of yttria stabilized tetragonal zirconia polycrystals. *Adv. Ceram. Mat.*, **1**(3) (1986) 259–63.

11 Sato, T. & Shimada, M., Control of the tetragonal to monoclinic phase transformation of yttria partially stabilized zirconia in hot water. *J. Mater. Sci.*, **20** (1985) 3988–92.

12 Winnubst, A. J. A. & Burggraaf, A. J., The ageing behaviour of ultra fine grained Y-TZP in hot water. In *Advances in*

Ceramics, Vol 24A, ed S Somiya, N Yamamoto & H Hanagida American Ceramic Society, Westerville, OH, 1988, pp 39–47

13 Sato, T & Shimada M, Transformation of ceria doped tetragonal zirconia polycrystals by annealing in water *Am Ceram Soc Bull*, **64** (1985) 1382–4

14 Tsukuma, K & Shimada, M, Strength, fracture toughness and Vickers hardness of CeO_2 stabilized tetragonal ZrO_2 polycrystals *J Mater Sci* **20** (1985) 1178–84

15 Duh J Dai, H & Hsu, W Synthesis and sintering behaviour in CeO_2 ZrO_2 ceramics *J Mater Sci* **23** (1988) 2786–91

16 Wakai F Murayama N Sakaguchi S Kato, H & Kimoda K Deformation of superplastic tetragonal ZrO_2 polycrystal In *Advances in Ceramics*, Vol 24B American Ceramic Society Westerville OH 1988 pp 583–93

17 Sato T Ohtaki S Endo, T & Shimada, M Improvement of thermal stability of yttria doped tetragonal zirconia polycrystals by alloying with various oxides *J High Technol Ceram* **2** (1986) 167–77

18 Hernandez M T Jurado, J R & Duran P Subeutectoid degradation of yttria stabilized tetragonal zirconia polycrystal and ceria doped yttria stabilized tetragonal zirconia polycrystal ceramics *J Am Ceram Soc* **74**(6) (1991) 1284–8

19 Theunissen G S A M Winnubst, A J A & Burggraaf A J Effect of dopants on sintering behaviour and stability of tetragonal zirconia ceramics *J Eur Ceram Soc* **9** (1992) 251–63

20 Boutz M M R, Winnubst, A J A, van Langerak B Kreuwel K & Burggraaf A J A The effect of ceria codoping on chemical stability and fracture toughness of Y TZP *J Mater Sci*

21 Hirano M & Inada H Fracture toughness, strength and Vickers hardness of yttria-ceria doped tetragonal zirconia alumina composites fabricated by hot isostatic pressing *J Mater Sci*, **26** (1991) 5047–52

22 Theunissen, G S A M Winnubst, A J A & Burggraaf A J Surface and grain boundary analysis of doped zirconia ceramics studied by AES and XPS *J Mater Sci* **27** (1992) 5057–66

23 Hwang S & Chen I Grain size control of tetragonal zirconia polycrystals using the space charge concept *J Am Ceram Soc*, **73**(11) (1990) 3269–77

24 Nieh T G & Wadsworth J Effect of grain size on superplastic behavior of Y TZP *Scripta Metall Mater* **24** (1990) 763–6

25 Boutz M M R Winnubst A J A, Burggraaf A J, Nauer, M & Carry C Low temperature superplastic flow of yttria stabilized tetragonal zirconia polycrystals In *Euro Ceramics II Vol 2* ed G Ziegler and H Hausner Deutsche Keramische Gesellschaft e V, Koln, 1991, pp 939–43

26 van de Graaf M A C G, ter Maat, J H H & Burggraaf, A J, Microstructure and sintering kinetics of highly reactive ZrO_2 Y_2O_3 ceramics *J Mater Sci*, **20** (1985) 1407–18

27 Kaliszewski M S & Heuer A H Alcohol interaction with zirconia powders *J Am Ceram Soc*, **73**(6) (1990) 1504–9

28 Groot Zevert W F M, Winnubst, A J A Theunissen G S A M & Burggraaf A J, Powder preparation and compaction behaviour of fine grained Y TZP *J Mater Sci* **25** (1990) 3449–55

29 Haberko K Characteristics and sintering behaviour of zirconia ultrafine powders *Ceramurgia Int*, **5**(4) (1979) 148–54

30 Lippens B C & de Boer, J H, Studies on pore systems in catalysts V The *t* method *J Catalysis*, **4** (1965) 319–23

31 Barett, E P Joyner, L G & Halenda, P P The determination of pore volume and area distributions in porous substances I Computations from nitrogen isotherms *J Am Chem Soc*, **73** (1951) 373–80

32 Schreiner, W N & Jenkins R, Profile fitting for quantitative analysis in powder diffraction *Adv X-ray Anal* **26** (1983) 141–7

33 Mendelson, M I, Average grain size in polycrystalline ceramics *J Am Ceram Soc*, **52**(8) (1969) 443–6

34 Boutz, M M R, Chen, C S Winnubst, A J A & Burggraaf, A J, Characterisation of grain boundaries in superplastically deformed Y TZP ceramics *J Am Ceram Soc*

35 Brook R J, Controlled grain growth In *Treatise on Materials Science and Technology* Vol 9 ed F Wang Academic Press, NY, 1976, pp 331–64

36 Greskovich C & Lay K W Grain growth in very porous Al_2O_3 compacts *J Am Ceram Soc* **55**(3) (1972) 142–6

37 Gregg S J & Sing, K S W, *Adsorption, Surface Area and Porosity* 2nd edn Academic Press, London, 1982

38 de Boer J H, The shapes of capillaries In *The Structure and Properties of Porous Materials* ed D H Everett & F S Stone Butterworth Scientific Publications 1958, pp 68–94

39 Lecloux, A & Pirard, J P, The importance of standard isotherms in the analysis of adsorption isotherms for determining the porous texture of solids *J Coll Interface Sci* **70**(2) (1979) 265–81

40 Kumar K P Nanostructured ceramic membranes Layer and texture formation Thesis University of Twente 1993

41 Mercera P D L van Ommen, J G Doesburg, E B M Burggraaf A J & Ross J R H Zirconia as a support for catalysts Evolution of the texture and structure on calcination in air *J Appl Catal*, **57** (1990) 127–48

42 Bannister M J, Shape sensitivity of initial sintering equations *J Am Ceram Soc* **51**(10) (1968) 548–53

43 Young W S & Cutler I B Initial sintering with constant rates of heating *J Am Ceram Soc*, **53**(12) (1970) 659–63

44 Woolfrey J L & Bannister M J, Nonisothermal techniques for studying initial stage sintering *J Am Ceram Soc* **55**(8) (1972) 390–4

45 Wang J & Raj, R Activation energy for the sintering of two phase alumina zirconia ceramics *J Am Ceram Soc*, **74**(8) (1991) 1959–63

46 Burggraaf A J & Winnubst, A J A, Segregation in oxide surfaces solid electrolytes and mixed conductors In *Surface and Near Surface Chemistry of Oxide Materials*, ed J Nowotny & L C Dufour Elsevier Science Publishers B V Amsterdam 1988, pp 449–77

47 Shannon R D *Acta Cryst* **A32** (1976) 751–67

48 Paparazzo E Ingo G M & Zacchetti, N X Ray induced reduction effects at CeO_2 surfaces an X ray photoelectron spectroscopy study *J Vac Sci Technol A* **9**(3) (1991) 1416–20

49 Lange, F F, Contributions of sintering and coarsening to densification a thermodynamic approach In *Advanced Ceramics III*, ed S Somiya Elsevier Applied Science London and New York, 1990, pp 57–70

50 Duran P Recio P Jurado, J R Pascual C & Moure, C, Preparation sintering and properties of translucent Er_2O_3 doped tetragonal zirconia *J Am Ceram Soc* **72**(11) (1989) 2088–93

51 Veringa H J Sintering models and the development of instabilities *J Mater Sci*, **26** (1991) 5985–95

52 Hahn H Logas, J & Averback R S Sintering characteristics of nanocrystalline TiO *J Mater Res*, **5**(3) (1990) 609–14

53 Akine M private communication 1992

54 Hernandez M T Jurado, J R & Duran, P, Influence of CeO_2 content on the electrical properties of Y_2O_3 TZP ceramics *Solid State Ionics*, **51** (1992) 147–56

Appendix

A general grain growth equation will be derived here for the case of heating with a constant rate β The terminology used and basic formulas are in accordance with Ref 35. The central assumption for

analysing grain growth kinetics is that the growth rate is directly proportional to the average rate v of grain boundary migration The average rate v can be written as a mobility (M)–force (F) product. The starting equation is therefore equal to:

$$\frac{dD}{dt} \sim v = MF \tag{A1}$$

The driving force for grain boundary migration is usually taken to be inversely proportional to the grain size

$$F = \frac{K}{D} \tag{A2}$$

The various parameters that characterize the rate limiting step are thus included in the mobility term.

The migration of the boundary can be controlled by (a) the boundary itself or (b) the migration of pores attached to the boundary In the case of boundary control the mobility of the boundary (M_b) must be inserted in eqn (A1)

$$v = M_b F \tag{A3}$$

In the case of pore control eqn (A1) may be written as

$$v = F\left(\frac{M_p}{N}\right) \tag{A4}$$

where M_p is the pore mobility and N the number of pores attached to the boundary.

To evaluate grain growth kinetics from M_p and eqn (A4) two further assumptions are necessary:

(1) the average pore size is related to the average grain size by $r \sim D$,
(2) the number of pores N is inversely proportional to the square of grain size ($N \sim 1/D^2$).

In Table 3 of Ref 35 the expressions for the mobilities are given for the various possible mechanisms. From this table, the above mentioned assumptions and eqns (A3)–(A4), it is clear that the force–mobility product can be written as the quotient of a function of temperature $g(T)$ and one of grain size $f(D)$

$$v = \frac{g(T)}{f(D)} \tag{A5}$$

The function $g(T)$ can be written for each mechanism i as

$$g_i(T) = K_i\left(\frac{\tilde{D}_i}{T}\right) \tag{A6}$$

where $\tilde{D}_i$ is the chemical diffusion coefficient for mass transport mechanism i The function $f(D)$ can be written as:

$$f(D) = D^{n-1} \tag{A7}$$

Inserting eqn (A5) into (A1) and integrating gives:

$$\int f(D)\,dD = \int g_i(T)\,dt \tag{A8}$$

During heating with a constant rate β temperature and time are coupled by:

$$T = T_0 + \beta t \tag{A9}$$

where T_0 is the starting temperature (room temperature in the present measurements). Instead of integrating the right-hand side of (A8) in time, as in the case of constant temperature, one now has to integrate in temperature

$$\int_{t_0}^{t} g_i(T)\,dt = \int_{T_0}^{T} \frac{g_i(T)}{\beta}\,dT \tag{A10}$$

Inserting eqn (6) and the relationship $\tilde{D} = \tilde{D}_0 \exp(-Q/RT)$ into eqn (A10) yields:

$$\int_{T_0}^{T} \frac{g_i(T)}{\beta}\,dT = \frac{K_i\tilde{D}_0}{\beta}\int_{T_0}^{T}\left(\exp\left(-\frac{Q}{RT}\right)/T\right)dT \tag{A11}$$

The integral from $T = 0$ to $T = T_0$ of the function $g_i(T)$ is vanishingly small and the integral from $T = T_0$ to $T = T$ in eqn (A11) can therefore be replaced by the integral from $T = 0$ to $T = T$ The integral in eqn (A11) can then be solved analytically, but this leads to the following inconvenient polynomial expression

$$\int_0^T \left(\exp\left(-\frac{Q}{RT}\right)/T\right)dT = \ln(T) - \sum_{k=1}^{\infty}\left\{\frac{1}{k\,k!}\left(-\frac{Q}{RT}\right)^k\right\} \tag{A12}$$

The terms with $k = 1$ in eqn (A12) cannot be neglected for realistic values of the activation energy Q (order-of-magnitude 10^2 kJ/mol) and the investigated temperature range (up to 1423 K). The solution of integral (A11) can, however, be well approximated by:

$$\int_0^T \left(\exp\left(-\frac{Q}{RT}\right)/T\right)dT \simeq \frac{RT}{Q}\exp\left(-\frac{Q}{RT}\right) \tag{A13}$$

The validity of this approximation can easily be recognized by differentiation of the right-hand side of eqn (A13), remembering that $R/Q \ll 1$. The validity has also been checked by numerically integrating eqn (A11) and comparing the outcome with that of eqn (A13)

The left-hand side of eqn (8) remains unchanged wrt the isothermal case and must be integrated from D_0 to D. The final equation to analyse grain growth kinetics during heating with a constant rate β is therefore equal to.

$$D^n - D_0^n = \frac{K_i RT}{\beta Q}\exp\left(-\frac{Q}{RT}\right) \tag{A14}$$

where K_i is a constant, RT has its usual meaning and Q is the apparent activation energy